Broad-band X-ray spectral analysis of the Seyfert 1 galaxy GRS 1734-292

Author(s):
Tortosa, A.; Marinucci, A.; Matt, G.; Bianchi, S.; La Franca, F.; Ballantyne, D.R.; Boorman, P.G.; Fabian, A.C.; Farrah, D.; Fuerst, F.; Gandhi, P.; Harrison, F.A.; Koss, Michael J.; Ricci, C.; Stern, D.; Ursini, F.; Walton, D.J.

Publication date:
2017-05

Permanent link:
https://doi.org/10.3929/ethz-b-000191844

Originally published in:
Monthly Notices of the Royal Astronomical Society 466(4), https://doi.org/10.1093/mnras/stw3301

Monthly Notices
of the
ROYAL ASTRONOMICAL SOCIETY

MNRAS **466,** 4193–4200 (2017)
Advance Access publication 2016 December 17

doi:10.1093/mnras/stw3301

Broad-band X-ray spectral analysis of the Seyfert 1 galaxy GRS 1734−292

A. Tortosa,[1]★ A. Marinucci,[1] G. Matt,[1] S. Bianchi,[1] F. La Franca,[1] D. R. Ballantyne,[2] P. G. Boorman,[3] A. C. Fabian,[4] D. Farrah,[5] F. Fuerst,[6] P. Gandhi,[3] F. A. Harrison,[6] M. J. Koss,[7] C. Ricci,[8,9] D. Stern,[10] F. Ursini[1,11,12] and D. J. Walton[6,10]

[1]*Dipartimento di Matematica e Fisica, Università degli Studi Roma Tre, via della Vasca Navale 84, I-00146 Roma, Italy*
[2]*Center for Relativistic Astrophysics, School of Physics, Georgia Institute of Technology, 837 State Street, Atlanta, GA 30332-0430, USA*
[3]*School of Physics and Astronomy, University of Southampton, Highfield, Southampton SO17 1BJ, UK*
[4]*Institute of Astronomy, Madingley Road, Cambridge CB3 OHA, UK*
[5]*Department of Physics, Virginia Tech, Blacksburg, VA 24061, USA*
[6]*Space Radiation Laboratory, California Institute of Technology, Pasadena, CA 91125, USA*
[7]*Institute for Astronomy, Department of Physics, ETH Zurich, Wolfgang-Pauli-Strasse 27, CH-8093 Zurich, Switzerland*
[8]*Instituto de Astrofísica, Facultad de Física, Pontificia Universidad Católica de Chile, Casilla 306, 8970117 Santiago 22, Chile*
[9]*EMBIGGEN Anillo, 8970117 Concepción, Chile*
[10]*Jet Propulsion Laboratory, California Institute of Technology, Pasadena, CA 91109, USA*
[11]*Univ. Grenoble Alpes, CNRS, IPAG, F-38000 Grenoble, France*
[12]*CNRS, IPAG, F-38000 Grenoble, France*

Accepted 2016 December 14. Received 2016 December 14; in original form 2016 September 8

ABSTRACT

We discuss the broad-band X-ray spectrum of GRS 1734−292 obtained from non-simultaneous *XMM–Newton* and *NuSTAR* (*Nuclear Spectroscopic Telescope Array*) observations, performed in 2009 and 2014, respectively. GRS1734−292 is a Seyfert 1 galaxy, located near the Galactic plane at $z = 0.0214$. The *NuSTAR* spectrum (3–80 keV) is dominated by a primary power-law continuum with $\Gamma = 1.65 \pm 0.05$ and a high-energy cut-off $E_c = 53^{+11}_{-8}$ keV, one of the lowest measured by *NuSTAR* in a Seyfert galaxy. Comptonization models show a temperature of the coronal plasma of $kT_e = 11.9^{+1.2}_{-0.9}$ keV and an optical depth, assuming a slab geometry, $\tau = 2.98^{+0.16}_{-0.19}$ or a similar temperature and $\tau = 6.7^{+0.3}_{-0.4}$ assuming a spherical geometry. The 2009 *XMM–Newton* spectrum is well described by a flatter intrinsic continuum ($\Gamma = 1.47^{+0.07}_{-0.03}$) and one absorption line due to Fe XXV Kα produced by a warm absorber. Both data sets show a modest iron Kα emission line at 6.4 keV and the associated Compton reflection, due to reprocessing from neutral circumnuclear material.

Key words: galaxies: active – galaxies: individual: GRS 1734−292 – galaxies: Seyfert – X-rays: galaxies.

1 INTRODUCTION

The primary X-ray emission in active galactic nuclei (AGNs) is believed to be produced in a compact hot region, located close to the supermassive black hole, and composed of a plasma of hot electrons: the corona (Haardt & Maraschi 1993). The optical/UV disc photons are scattered up to the X-ray band due to the inverse Compton effect in this hot corona. The Comptonization leads to a power-law continuum, extending up to energies determined by the plasma electron temperature (kT_e; Rybicki & Lightman 1979), where a cut-off occurs. The power-law index is directly related to the temperature and optical depth of the plasma of hot electrons responsible for the power-law emission while the cut-off energy is mainly related to the electron temperature.

Pre-*NuSTAR* (*Nuclear Spectroscopic Telescope Array*: Harrison et al. 2013) measurements of cut-off energies ranged between 50 and 300 keV (e.g. Perola et al. 2002; Dadina 2007; Malizia et al. 2014). *NuSTAR*'s high sensitivity in hard X-rays, allowing for the first time source-dominated observations of Seyfert galaxies above 10 keV, has recently led to high-energy cut-off measurements from 100 keV to more than 350 keV for several nearby Seyfert galaxies (see Ballantyne et al. 2014; Brenneman et al. 2014; Marinucci et al. 2014; Baloković et al. 2015; Matt et al. 2015), plus a number of significant lower limits (Fabian et al. 2015).

The nearby ($z = 0.0214$, corresponding to a distance of 87 Mpc) Seyfert Galaxy GRS 1734−292 is a good candidate for such measurements. With an X-ray luminosity approaching $\sim 10^{44}$ erg s^{-1} in the 0.5–4.5 keV energy band (Martí et al. 1998), it is one of the most

★E-mail: tortosa@fis.uniroma3.it

luminous AGNs within 100 Mpc (Piccinotti et al. 1982; Sazonov & Revnivtsev 2004).

GRS 1734−292 was originally discovered by the Coded-mask X-ray telescope aboard the *GRANAT* satellite (Pavlinsky, Grebenev & Sunyæv 1992) and is located only 1.°8 from the Galactic Centre. The spectrum between 4 and 20 keV was well described by a power law with a photon index $\Gamma \sim 2$ and a total hydrogen column density in excess of 10^{22} cm^{-2}. These characteristics, with the inferred X-ray luminosity $\sim 10^{36}$erg s^{-1} assuming the Galactic Centre distance, were consistent with the source being a Galactic X-ray binary. Martí et al. (1998) revealed that the optical spectrum of GRS 1734−292 is dominated by strong and very broad emission from blended H and [N II] lines, but also other emission lines, such as [O I], [O II] and [S II], all at a redshift of 0.0214. Moreover, the radio, infrared and optical counterparts of GRS 1734−292 are all consistent with a Seyfert 1 galaxy. In particular, the radio counterpart is a double-sided synchrotron jet of 5 arcsec extent. At the distance of 87 Mpc, this corresponds to a size of 2 kpc. With a radio luminosity of $L_{\rm rad} \simeq 7 \times 10^{39}$erg s^{-1} in the 0.1–100 GHz band and an X-ray luminosity $L_{\rm X} \simeq 1 \times 10^{44}$ erg s^{-1} in the 0.5–4.5 keV band, GRS 1734−292 is a radio-quiet AGN (Laor & Behar 2008).

The hard X-ray spectrum of GRS 1734−292 was measured for the first time with the Imager on Board the Integral Satellite (IBIS) telescope onboard the *INTEGRAL* observatory (Sazonov et al. 2004). Afterwards, it was also analysed by Molina et al. (2013). The composite X-ray (2–200 keV) spectrum with the *ASCA*/Gas Imaging Scintillation observation at 2–10 keV (Sakano et al. 2002) is typical of Seyfert galaxies, well described by a power law of $\Gamma \sim 1.8$ modified by Compton reflection at 10–100 keV and an exponential cut-off at $E_{\rm c} > 100$–200 keV.

GRS 1734−292 was detected also in 70 months of observations by the Burst Alert Telescope (BAT) hard X-ray detector (Barthelmy et al. 2005) on the *Swift* gamma-ray burst observatory (Gehrels et al. 2004). The spectral analysis (Baumgartner et al. 2011) showed a power law with a photon index $\Gamma \sim 2.18 \pm 0.07$ and a luminosity of $L \sim 1$–2×10^{44} erg s^{-1} in the 14–195 keV band.

Guainazzi et al. (2011) analysed the *XMM–Newton* observation in their GREDOS (General Relativity Effects Detected in Obscured Sources) sample and found that the spectrum is well described by a power law with a rather flat spectral index $\Gamma = 1.41^{+0.01}_{-0.02}$. They found a hydrogen column density of $N_{\rm H} = 1.41 \pm 0.02 \times 10^{22}$ cm^{-2}. From the spectral analysis of the simultaneous *XMM–Newton* and *INTEGRAL*/IBIS–*Swift*/BAT observations, Malizia et al. (2014) found a primary continuum with a power-law index $\Gamma = 1.55^{+0.15}_{-0.08}$ and a cut-off energy $E_{\rm c} = 58^{+24}_{-7}$ keV.

This work focuses on investigating the broad-band X-ray spectrum of GRS 1734−292 and in particular the physical properties of the corona. In Section 2, we discuss the *XMM–Newton* and *NuSTAR* observations and data reduction. In Section 3, we present a re-analysis of the 2009 *XMM–Newton* observation together with a new *NuSTAR* observation of GRS 1734−292. We discuss our results and summarize our conclusions in Section 4. In Appendix A, a measure of the width of the broad Hα λ6563 component, to infer the black hole mass via an updated virial-based, single-epoch relation, is presented.

2 OBSERVATIONS AND DATA REDUCTION

2.1 *NuSTAR*

GRS 1734−292 was observed by *NuSTAR* with its two co-aligned X-ray telescopes Focal Plane Modules A and B (FPMA and FPMB, respectively) on 2014 September 16, for a total elapsed time of 43 ks. The level 1 data products were processed with the *NuSTAR* Data Analysis Software (NUSTARDAS) package (v. 1.3.0). Cleaned event files (level 2 data products) were produced and calibrated using standard filtering criteria with the NUPIPELINE task and the latest calibration files available in the *NuSTAR* calibration data base (CALDB 20150316). The extraction radii of the circular region for source and background spectra were 1.5 arcmin each; there is no other bright X-ray source within 1.5 arcmin from GRS 1734 and no other sources were present in the background region. The net exposure times after this process were 20.3 ks for both FPMA and B. The two spectra were binned in order to oversample the instrumental resolution by at least a factor of 2.5 and to have a signal-to-noise ratio (SNR) greater than 3 in each spectral channel.

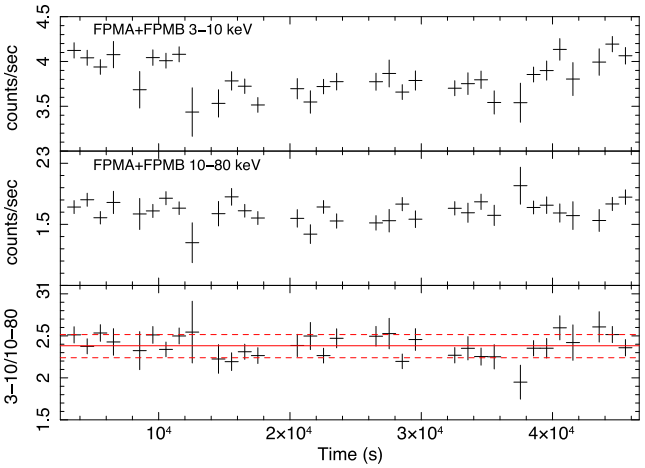

Figure 1. Top panel: *NuSTAR* FPMA+B light curve in the 3–10 keV energy band; middle panel: *NuSTAR* FPMA+B light curve in the 10–80 keV energy band; bottom panel: ratio between 3–10 keV and 10–80 keV *NuSTAR* light curves; the red solid and dashed lines indicate the mean and standard deviation, respectively.

Since no spectral variation (less than 10 per cent) is found in the ratio between the 3–10 and 10–80 keV count rates (see Fig. 1), we decided to use time-averaged spectra.

Since GRS 1734−292 lies very low on the galactic plane, the *NuSTAR* observation is moderately affected by stray light, due to sources off the field of view. This effect is more significant in the FPMB detector: a 50 ± 2 per cent increase in the background count rate is observed below 7 keV, with respect to the FPMA. We tried to extract the background spectra from different regions and no differences are found. Since the point source falls within the stray light region in both the detectors and the background is hence properly subtracted, this effect is not relevant to our data analysis. As a last check, we verified that no spectral difference arises between the two *NuSTAR* background subtracted spectra: they perfectly agree within cross-calibration uncertainties.

2.2 *XMM–Newton*

GRS 1734−292 was also observed with *XMM–Newton* on 2009 February 26 with the European Photon Imaging Cameras (EPIC) CCD cameras, which are comprised of the pn detector (Strüder et al. 2001) and the two Metal-Oxide-Semiconductor structure (MOS) units (Turner et al. 2001). The cameras were operated in large window and thin filter mode, for a total elapsed time of 18 ks. The extraction radii and the optimal time cuts for flaring particle

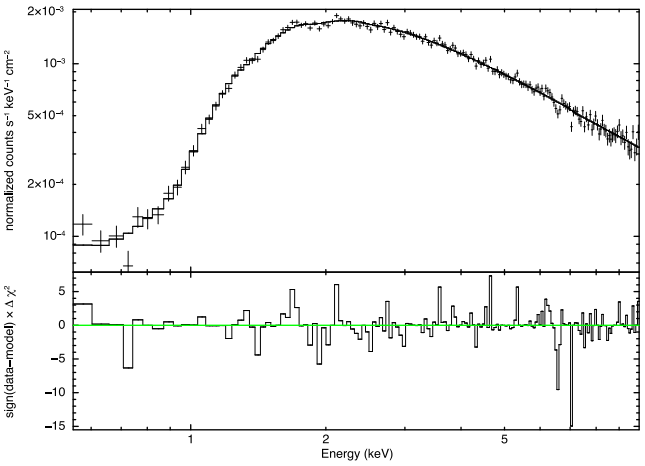

Figure 2. Data and residuals for the *XMM–Newton* spectrum when no Gaussian lines are included in the model.

background were computed with SAS 15 (Gabriel et al. 2004) via an iterative process that maximizes the SNR, similar to the approach described in Piconcelli et al. (2004). The resulting optimal extraction radius was 40 arcsec and the background spectra were extracted from source-free circular regions with radii of ∼50 arcsec for both the EPIC and the two MOS. EPIC spectra had a net exposure time of 13 ks, the MOS spectra had both a net exposure time of 15 ks. EPIC and MOS spectra were binned in order to oversample the instrumental resolution by at least a factor of 3 and to have no less than 30 counts in each background-subtracted spectral channel. Data from the MOS detectors are not included in our analysis unless stated otherwise.

3 SPECTRAL ANALYSIS

The spectral analysis has been performed with the XSPEC 12.9.0 software package (Arnaud 1996). Throughout the paper, errors correspond to the 90 per cent confidence level for one interesting parameter ($\Delta\chi^2 = 2.7$), if not stated otherwise. The cosmological parameters $H_0 = 70\,\mathrm{km\,s^{-1}\,Mpc^{-1}}$, $\Omega_\Lambda = 0.73$ and $\Omega_\mathrm{m} = 0.27$ are adopted.

3.1 Re-analysis of the *XMM–Newton* data

We started our data analysis by fitting the 0.5–10 keV *XMM–Newton* spectrum with a model[1] composed of a power law absorbed by the Galactic column density $N_\mathrm{H} = 7.57 \times 10^{21}\ \mathrm{cm^{-2}}$, as derived from H I maps (Kalberla et al. 2005), and an additional intrinsic absorber at the redshift of the source, found to be $0.84 \pm 0.03 \times 10^{22}\ \mathrm{cm^{-2}}$. This yielded a poor fit with $\chi^2 = 242$ for 163 degrees of freedom (d.o.f.). Since the data reveal a slight excess at energies <1 keV, we added a MEKAL thermal plasma component[2] (Mewe, Gronenschild & van denOord 1985), absorbed only by Galactic gas. We fixed the chemical abundance of metals to solar. The χ^2 is 209 for 161 d.o.f. for a thermal plasma temperature of $kT = 0.14^{+0.22}_{-0.05}$ keV and a 0.5–2 keV luminosity of $\sim 2.7 \pm 0.7 \times 10^{42}\ \mathrm{erg\,s^{-1}}$. Some residuals are however evident around 6–7.5 keV (see Fig. 2).

Therefore, we added a narrow Gaussian line[3] at 6.4 keV, corresponding to the neutral iron Kα emission line, which is a typical feature in Seyfert galaxies (Nandra & George 1994). We found the centroid value of the line to be 6.36 ± 0.07 keV and the fit slightly improved: $\chi^2 = 202$ for 159 d.o.f., with a $\frac{\Delta\chi^2}{\Delta\mathrm{d.o.f.}} = 3.5$ and a null hypothesis probability of 4.7×10^{-2} according to the *F*-test. The iron Kα emission line shows a flux of $1.4 \pm 0.8 \times 10^{-5}\ \mathrm{ph\,cm^{-2}\,s^{-1}}$ and an equivalent width of 20 ± 13 eV. We then added an absorption Gaussian line.[4,5] The flux and the line equivalent width of this absorption line were $2.1 \pm 0.8 \times 10^{-5}\ \mathrm{ph\,cm^{-2}\,s^{-1}}$ and 31 ± 12 eV, respectively. The centroid energy of this absorption line is consistent with the K-shell transition of Fe XXV ions. We tried to fit this component with a warm-absorber (WA) model,[6] using an ad hoc table produced with the photoionization code CLOUDY C13.03 (most recently described by Ferland et al. 2013). We found an ionization parameter of $\xi_i = 1778.3^{+2.7}_{-1.6}\ \mathrm{erg\,cm\,s^{-1}}$ and a column density $N_\mathrm{H} = 5.01 \pm 3.2 \times 10^{22}\ \mathrm{cm^{-2}}$. The upper limit to the velocity of the emitting material is $v_\mathrm{max} = 5300\,\mathrm{km\,s^{-1}}$. The χ^2 is 186 for 157 d.o.f.. To check the possibility that the absorption features are due to a collisional ionized gas, we fitted the data using the hotabs model in the warmabs code (Kallman & Bautista 2001) instead of the WA model. The fit is equivalent from a statistical point of view. We found a temperature of the gas of 0.85 ± 0.12 keV and a column density of $7.1 \pm 5.0 \times 10^{21}\ \mathrm{cm^{-2}}$. Further residuals around 7.2 keV suggested to add another Gaussian absorption line.[7] The inclusion of this component leads to a $\chi^2/\mathrm{d.o.f.} = 178/155 = 1.14$ (*F*-test null hypothesis probability 2.2×10^{-2}). The fit gives a centroid energy of $7.19^{+0.07}_{-0.09}$ keV, with a flux of $1.3 \pm 0.8 \times 10^{-5}\ \mathrm{ph\,cm^{-2}\,s^{-1}}$ and a line equivalent width (EW) of 28 ± 14 eV. An absorption line with this centroid energy is possibly a blueshifted line associated with the transition of Fe XXVI ions (rest-frame energy: 6.966 keV) produced by a material with a velocity of $9500\,\mathrm{km\,s^{-1}} \simeq 0.03c$. This is the lower limit of the range of velocities for Ultra Fast Outflows (Tombesi et al. 2010). To verify the presence of this line, we fitted the pn and the MOS spectra simultaneously with the same model. We tied all of the MOS parameters to the pn values. The normalizations of the two Gaussian lines and the normalization of the power law of the MOS spectra are tied together but are free to vary. The χ^2 of the fit is 461 for 427 d.o.f. The fit with the MOS data confirms the presence of the absorption line due to Fe XXV Kα ions produced by a WA, but not that at 7.2 keV. In fact, the upper limit to the flux of the latter line is $3.16 \times 10^{-6}\ \mathrm{ph\,cm^{-2}\,s^{-1}}$ at 90 per cent confidence level. In the following fits, therefore, this line will not be included.

We found that the photon index of the primary X-ray continuum is $\Gamma = 1.47 \pm 0.03$. This (see footnote 6) is our best fit and we will use it as the baseline model when adding the *NuSTAR* data.

3.2 Adding *NuSTAR* data

We started the analysis of the 3–80 keV *NuSTAR* (FPMA and FPMB) spectra fitting the data together with the *XMM–Newton*

[1] XSPEC model: TBabs * zwabs * powerlaw.
[2] XSPEC model: TBabs * (mekal + zwabs * powerlaw).
[3] XSPEC model: TBabs * (mekal + zwabs * (zgauss + powerlaw)).
[4] XSPEC model: TBabs*(mekal + zwabs*(zgauss + zgauss + powerlaw)), suggested by the presence of negative residuals around 6.7 keV. We found a centroid value for this line of 6.69 ± 0.05 keV; the χ^2 is 187 for 157 d.o.f., with a $\frac{\Delta\chi^2}{\Delta\mathrm{d.o.f.}} = 7.5$ and a null hypothesis probability of 1.5×10^{-3} according to the *F*-test.
[5] In principle, the *F*-test is not a reliable test for the significance of emission or absorption lines, but it can be used if their normalizations are allowed to be negative and positive (Protassov et al. 2002).
[6] XSPEC model: TBabs * (mekal + mtable{cloudy.fits} * zwabs * (zgauss + powerlaw)).
[7] XSPEC model: TBabs * (mekal + mtable{cloudy.fits} * zwabs * (zgauss + zgauss + powerlaw)).

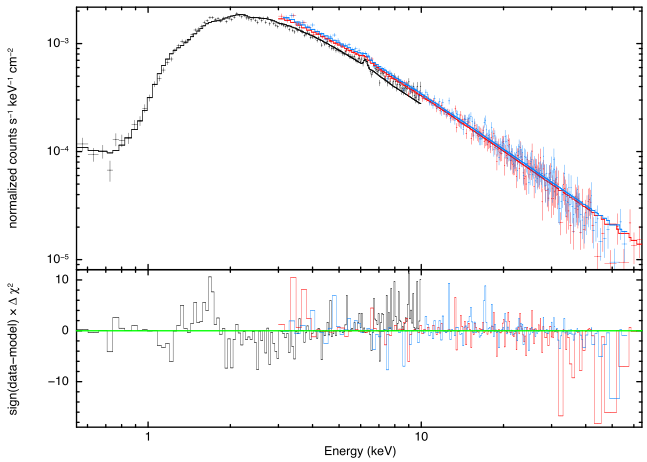

Figure 3. Data, fit model (top panel) and residuals (bottom panel) for *XMM–Newton* (black) and *NuSTAR* FPMA (red) and FPMB (in blue) spectra when the parameters are all tied to the best-fitting parameters from the *XMM–Newton* spectral fit.

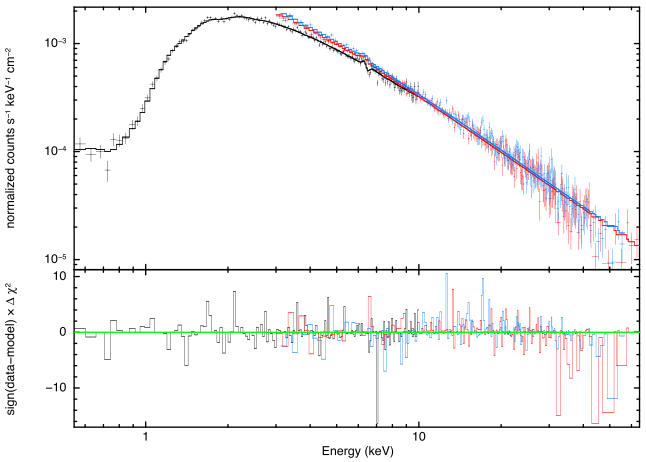

Figure 4. Data, fit model (top panel) and residuals (bottom panel) for *XMM–Newton* (black) and *NuSTAR* FPMA (red) and FPMB (blue) spectra when the power law in the model is not corrected by a high-energy cut-off. The photon indices of *XMM* and *NuSTAR* are left free to vary.

best fit found previously. We left all the parameters, apart from the normalizations of the various components, tied to the *XMM–Newton* best-fitting parameters. The *XMM–Newton* and the *NuSTAR* FPMA calibration constants are fixed to 1.0 (given the non-simultaneity of the two observations, any mismatch between the two instruments cannot be separated from intrinsic variations) while we left the *NuSTAR* FPMB cross-calibration constant free to vary. The value found for the constant is 1.004. The χ^2 for this fit is 830 for 544 d.o.f.. The spectral slope shows a different trend for the power law from the two observations (see Fig. 3) so we left the two photon indices, which are related to two different observations, free to vary. We kept tied the emission and absorption line centroid energies to the values found by *XMM–Newton* due to the lower spectral resolution of *NuSTAR*. We found that the *NuSTAR* photon index is steeper than the *XMM–Newton* one ($\Gamma = 1.65 \pm 0.05$). The fit leads to a χ^2/d.o.f. $= 662/543 = 1.22$. Re-analysing *Swift*/BAT observation from the *Swift* BAT 70-Month Hard X-ray Survey (NASA's Archive of Data on Energetic Phenomena),[8] we found a photon index $\Gamma = 2.18 \pm 0.07$ consistent with (Baumgartner et al. 2011). Adding a high-energy cut-off, however, we found a flatter photon index $\Gamma = 1.8 \pm 0.3$ and a high-energy cut-off value of $E_c = 110^{+300}_{-50}$ keV. The average *Swift*/BAT flux is higher than the *NuSTAR* one, which in turn is higher than the *XMM–Newton* one. The source therefore shows the softer-when-brighter behaviour (Shemmer et al. 2006; Sobolewska & Papadakis 2009), which is typical for Seyfert Galaxies.

Back to the *NuSTAR* data analysis, looking at the residuals above ∼40 keV (see Fig. 4) the presence of a high-energy cut-off is suggested, so we replaced the power-law component with a power law corrected by a high-energy exponential roll-off (CUTOFFPL model in XSPEC).[9] The fit improved significantly (χ^2/d.o.f. $= 556/541 = 1.1$); we found for the *NuSTAR* spectra $\Gamma = 1.58 \pm 0.04$ with the cut-off energy $E_c = 60^{+17}_{-9}$ keV and $\Gamma = 1.40^{+0.06}_{-0.09}$ for the *XMM–Newton* spectrum with a lower limit for the cut-off energy at 90 keV.

[8] http://swift.gsfc.nasa.gov/results/bs70mon/SWIFT_J1801.1-2544

[9] XSPEC model: constant * TBabs * (mekal + mtable{cloudy.fits} * zwabs * (zgauss + cutoffpl)).

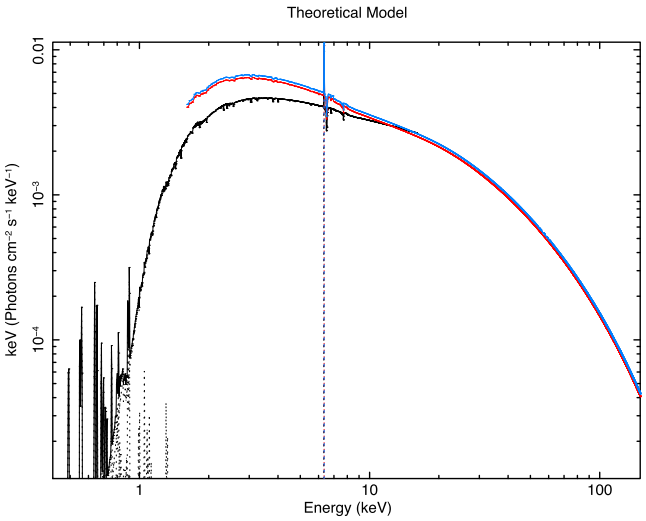

Figure 5. Best-fitting phenomenological model including the soft excess component, two narrow Gaussian lines, the WA and a cut-off power law reflected from neutral material (PEXRAV model), all absorbed by the Galactic column density and an intrinsic absorber.

We then included a cold reflection component in both the data sets, using the PEXRAV model (Magdziarz & Zdziarski 1995) in XSPEC, to test for the presence of a Compton reflection continuum. We fixed all element abundances to solar values and fixed the inclination angle to the default value ($\cos i = 0.45$, $i \sim 60°$). Because in the previous fit we found only a lower limit to the high-energy cut-off in the *XMM–Newton* spectrum, for the sake of simplicity we fixed it to 1 MeV. The model used in the fit is shown in Fig. 5. Data and residuals are shown in Fig. 6, while the best-fitting parameters are shown in Table 1. The photon index and high-energy cut-off are now $\Gamma = 1.65 \pm 0.05$ and $E_c = 53^{+11}_{-8}$ keV. The reflection fraction R is 0.48 ± 0.22. In the left-hand panel of Fig. 7, the contour plot of the cut-off energy versus the photon index of the power law for the *NuSTAR* observation is shown, while in the right-hand panel we show the contour plot of the high-energy cut-off versus the reflection fraction.

The fit shows a weaker iron line with respect to what we expected from the Compton hump. Replacing the PEXRAV model with a

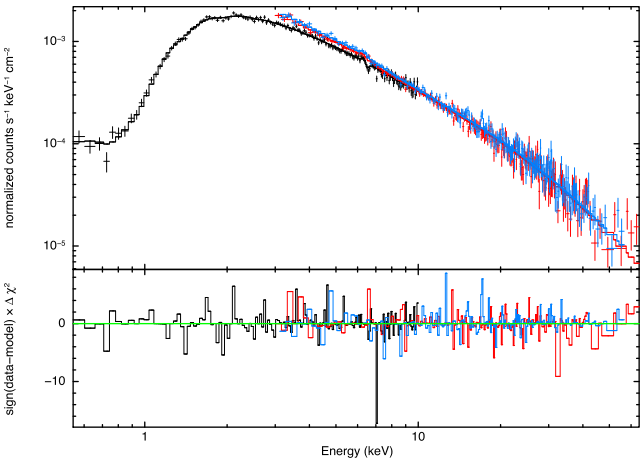

Figure 6. Data and best-fitting model extrapolated from *XMM–Newton* (black) and *NuSTAR* FPMA (red) and FPMB (blue) spectra when model in Fig. 5 is used; see text for more details. Residuals are shown in lower panel.

Table 1. Best-fitting parameters for the phenomenological model including PEXRAV and two Gaussian lines (line 1 at 6.4 keV and line 2 at 6.68 keV, obtained from the *XMM–Newton* spectrum). Errors are at 90 per cent confidence levels. The χ^2/d.o.f. value is 580/540 = 1.07.

Parameter	*XMM–Newton*	*NuSTAR*
$N_{\rm H}$ (10^{22} cm^{-2})	0.88 ± 0.05	0.88^a
Γ	$1.47^{+0.07}_{-0.03}$	1.65 ± 0.05
$E_{\rm c}$ (keV)	1000^b	53^{+11}_{-8}
R	<0.6	0.48 ± 0.22
F_{2-10} (10^{-11} erg cm^{-2} s^{-1})	$5.12^{+0.15}_{-0.08}$	$6.62^{+0.02}_{-0.08}$
L_{2-10} (10^{43} erg s^{-1})	5.23 ± 0.03	6.67 ± 0.04
F_{10-80} (10^{-10} erg cm^{-2} s^{-1})	–	1.25 ± 0.01
L_{10-80} (10^{44} erg s^{-1})	–	1.29 ± 0.05
F_1 (10^{-5} ph cm^{-2} s^{-1})	1.37 ± 0.84	3.93 ± 1.91
EW$_1$ (eV)	20 ± 13	50 ± 31
F_2 (10^{-5} ph cm^{-2} s^{-1})	2.06 ± 0.77	0.75 ± 1.86
EW$_2$ (eV)	-31 ± 12	<28

Notes. [a]Tied parameter.
[b]Fixed parameter.

self-consistent model that includes the Fe Kα line, such as the PEXMON model[10] (Nandra et al. 2007), with the relative iron abundance left free to vary, a value of 0.6 ± 0.3 is found for this parameter ($\chi^2 = 585$ for 542 d.o.f.)

In order to test for the presence of a relativistic component, we fitted the data with the RELXILL model[11] (García et al. 2014). Since the black hole spin parameter was not constrained, we assumed $a = 0.998$. We fixed the reflection fraction parameter to the best-fitting values found with the previous best-fitting model (see Table 1). Including the relativistic effects provides no improvement in the fit, implying that no relativistic component is required by the data.

[10] XSPEC model: constant * TBabs * (mekal + mtable{cloudy.fits} * zwabs * pexmon).
[11] XSPEC model: constant * TBabs * (mekal + mtable{cloudy.fits} * zwabs * relxill).

3.3 Comptonization features

Finally, assuming that the primary emission is due to Comptonization of thermal disc photons in a hot corona, we estimated the coronal parameters using an analytical Comptonization model. The temperature is expected to be related to the cut-off energy by $E_{\rm c} = 2$–$3 \times kT_{\rm e}$ (Petrucci et al. 2000, 2001); so, for such a low value of the cut-off energy (53^{+11}_{-8} keV), we expect a low value for the coronal temperature, and a high value for the optical depth to account for the flat spectrum. We fitted the *NuSTAR* spectra with the COMPTT model (Titarchuk 1994), adding the reflection component computed by PEXRAV with two Gaussian lines[12] (the iron Kα emission line and the absorption line due to Fe XXV Kα ions). Because of the low *NuSTAR* spectral resolution, we fixed the centroid energies of the lines to the values found in the best fit of the *XMM–Newton* data. In this model, the seed photon spectrum is a Wien law; we fixed the temperature to the maximum temperature of the accretion disc, which in this case, for Shakura & Sunyæv (1973) disc, is 4 eV, given the black hole mass of $\sim 3 \times 10^8$ solar masses (see Appendix A). In the case of a slab geometry of the corona, we found a coronal temperature $kT_{\rm e} = 12.1^{+1.8}_{-1.2}$ keV and an optical depth $\tau = 2.8^{+0.2}_{-0.3}$. The fit is good, with a χ^2 of 411 for 383 d.o.f.. For the case of a spherical geometry, we found a statistically equivalent fit. The value of the coronal temperature is about the same, while the optical depth is higher by almost a factor of 2: $\tau = 6.3^{+0.4}_{-0.5}$. The difference is primarily due to the different meaning of this parameter in the two geometries: the optical depth for a slab geometry is the average of optical depth values along the different directions, so it is lower than the effective value, while that for a sphere is the radial one (see Titarchuk 1994 for a more detailed description). The contour plots of the coronal temperature versus the optical depth obtained with the two different geometries are shown in Fig. 8.

We did not try to fit the Comptonization with the COMPPS model because the optical depth values obtained with the COMPTT model are too high and they do not fall within the region of parameter space where the numerical COMPPS method produces reasonable results (see Poutanen & Svensson 1996 for more details).

4 DISCUSSION AND CONCLUSIONS

We have presented an analysis of non-simultaneous *XMM–Newton* and *NuSTAR* observations of the Seyfert 1 galaxy GRS 1734−292. The spectral slope of the primary power law is different between the two observations, being very flat in the *XMM–Newton* observation ($\Gamma \sim 1.47$, consistent with the values found by Guainazzi et al. 2011), while it is more typical of a Seyfert galaxy in the *NuSTAR* observation ($\Gamma \sim 1.65$), when the source was a factor of ∼1.3 brighter. The variation of the spectral photon index could be associated with a variation of the coronal parameters and in particular of the optical depth.

The 2–10 keV absorption-corrected luminosity from the *XMM–Newton* observation is $L_{2-10} = 5.23 \pm 0.03 \times 10^{43}$ erg s^{-1}. Using the 2–10 keV bolometric correction of Marconi et al. (2004), we estimate the bolometric luminosity to be $L_{\rm bol} = 1.45 \times 10^{45}$erg s^{-1}. From the bolometric luminosity, with the black hole mass as in Appendix A, we estimate the $L_{\rm bol}/L_{\rm Edd}$ ratio to be 0.033.

The presence of an iron Kα emission line at 6.4 keV, albeit weak, is confirmed. We found also one absorption line, with a centroid

[12] XSPEC model: constant * TBabs * zwabs * (compTT + zgauss + zgauss + pexrav).

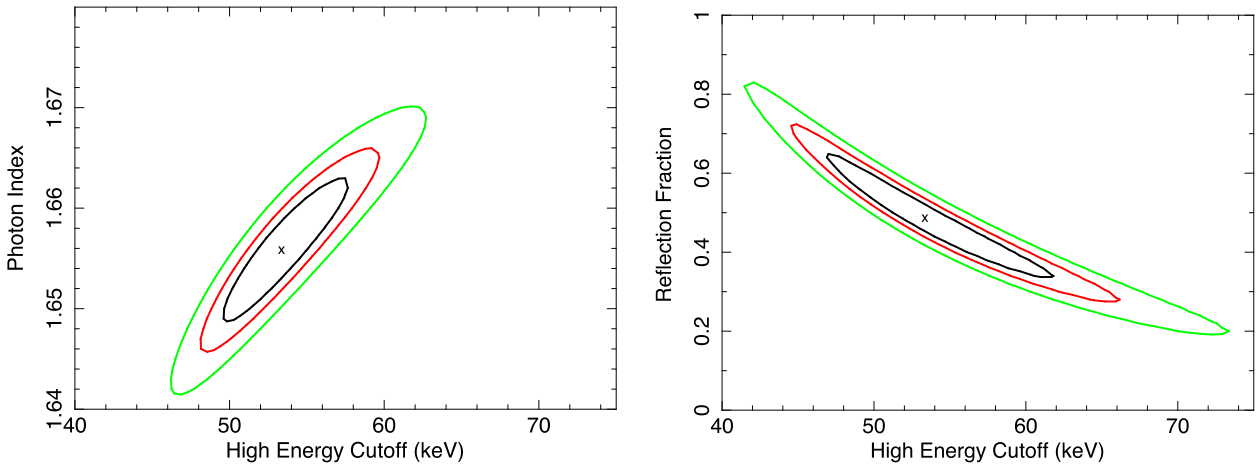

Figure 7. E_c–Γ contour plot (left-hand panel) and E_c–R contour plot (right-hand panel) for the *NuSTAR* observation. The solid black, red and green curves refer to the 68, 90 and 99 per cent confidence levels, respectively. The X represents the best-fitting value of the parameters.

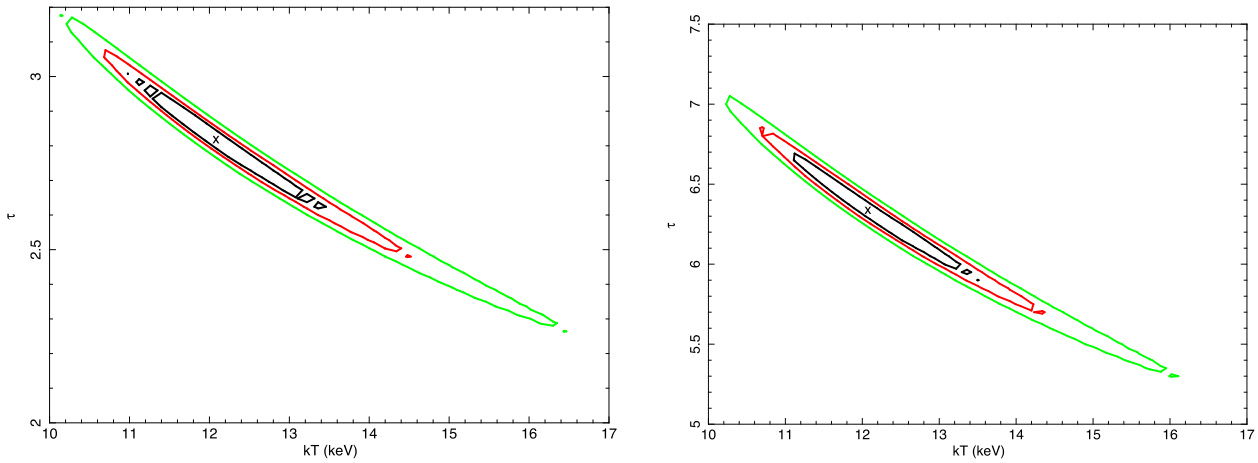

Figure 8. Coronal temperature versus optical depth contour plot in the case of slab geometry (left-hand panel) and spherical geometry (right-hand panel) for the *NuSTAR* observation when the COMPTT model is used to fit the data. The solid black, red and green curves refer to the 68, 90 and 99 per cent confidence levels, respectively. The X represents the best-fitting value of the parameters.

energy at around 6.69 keV, which is consistent with the energy expected for the K-shell transition of Fe XXV ions. The cut-off energy is 53^{+11}_{-8} keV, fully consistent with that found by Malizia et al. (2014). This is the lowest value found so far by *NuSTAR* in a Seyfert galaxy together with Mrk 335 (Keek & Ballantyne 2016); comparable or even lower values are found in stellar-mass accreting black holes (Miller, Parker & Fuerst 2013; Miller, Tomsick & Bachetti 2015). We estimated the coronal parameters by fitting the *NuSTAR* data with the COMPTT Comptonization model, finding a coronal temperature of $kT_e = 12.1^{+1.8}_{-1.28}$ keV and an optical depth $\tau = 2.8^{+0.2}_{-0.3}$ assuming a slab geometry or a similar temperature and $\tau = 6.38^{+0.4}_{-0.5}$ assuming a spherical geometry. Of course, we are implicitly assuming a simple picture in which the corona is a single temperature zone, which may not be the case if the heating is localized, as e.g. in the case of magnetic reconnection.

We used these values to put GRS 1734−292 in the compactness–temperature (Θ_e–ℓ) diagram (Fabian et al. 2015, and references therein). Here, $\Theta_e = kT_e/m_ec^2$ is the electron temperature normalized to the electron rest energy and ℓ is the dimensionless compactness parameter (Fabian et al. 2015):

$$\ell = \frac{L}{R}\frac{\sigma_T}{m_ec^3}, \quad (1)$$

where L is the luminosity and R is the radius of the corona (assumed spherical). We obtain $\Theta_e = 0.023^{+0.004}_{-0.002}$. To compute the compactness parameter, following Fabian et al. (2015), we adopted the luminosity of the power-law component extrapolated to the 0.1–200 keV band; since no measurement exists for the radius, we assume a value of 10 gravitational radii R_g. We found $\ell = 13.3 \pm 0.3(R_{10})^{-1}$ where R_{10} is the ratio between the radius and $10R_g$.

As obvious, given the low coronal temperature, GRS 1734−292 is located far away from the region of pair production in the Θ_e–ℓ plane, and is also located well below the e^-–e^- coupling line (i.e. the line below which the electron–electron coupling time-scale is shorter than the Compton cooling time-scale). This should ensure that the electron population is thermalized. It is instead located close to the e^-–p coupling line, below which the electron–proton coupling time-scale is shorter than the Compton cooling time-scale. It is interesting to note that no sources among those analized by Fabian et al. (2015) lie definitely below the e^-–p line, while a number of them lie around or just above (see fig. 4 in their paper). This line seems to set a physical boundary. If the electron population cools by Compton scattering its temperature decrease until electron-proton coupling becomes important and until the transfer of energy from protons to electrons becomes effective. This is not a completely

self-consistent picture, as the electron–proton coupling line was calculated assuming that the electron and proton temperatures (normalized to their mass), Θ_e and Θ_p, are the same (Fabian 1994), which is unlikely when Compton cooling dominates. Moreover, the dependence of the coupling time on Θ_e is small as soon as the two temperatures are decoupled and the proton temperature is the largest. Time-dependent, detailed calculations with realistic heating and energy redistribution mechanisms are required to assess how effective this feedback may be.

Only a few AGNs in the Fabian et al. (2015) compilation have temperatures as low as that of GRS 1734−292, and none among those observed by *NuSTAR*. We note that the accretion rate of GRS 1734−292 is only a few per cent of the Eddington limit, so the effectiveness of the cooling mechanism cannot be related to a particularly strong radiation field. It may, however, be at least partly related to the high value of the optical depth τ. A seed photon coming from the disc, in fact, will undergo more than one scattering before leaving the corona, thereby reducing the electron temperature. Indeed, models predict an anticorrelation between coronal temperature and optical depth (see e.g. Petrucci et al. 2001 for a calculation based on the two-phase model of Haardt & Maraschi 1993: note that values not too different from ours are predicted). The reason for the unusually large value of the optical depth is unclear (but see Keek & Ballantyne 2016 for evidence of an increase of the optical depth with decreasing Eddington ratio in Mrk 335) and difficult to assess given our poor knowledge of the processes that originate the corona and of the mechanisms that transfer the energy there. But with the increasing amount of high-quality spectra from *NuSTAR*, progressively populating this parameter space, it is at least possible to start seriously pondering these questions.

ACKNOWLEDGEMENTS

We thank the anonymous referee for comments that helped improving the clarity of the paper. This work made use of data from the *NuSTAR* mission, a project led by the California Institute of Technology, managed by the Jet Propulsion Laboratory, and funded by the National Aeronautics and Space Administration. We thank the *NuSTAR* Operations, Software and Calibration teams for support with the execution and analysis of these observations. This research has made use of the*NuSTAR* Data Analysis Software (NUSTARDAS) jointly developed by the ASI Science Data Center (ASDC, Italy) and the California Institute of Technology (USA). The work is also based on observations obtained with *XMM–Newton*, an ESA science mission with instruments and contributions directly funded by ESA Member States and the USA (NASA). AT, AM, GM and FU acknowledge financial support from Italian Space Agency under grant ASI/INAF I/037/12/0-011/13 and SB under grant ASI-INAF I/037/12/P1. AT, AM, SB and GM acknowledge financial support from the European Union Seventh Framework Programme (FP7/2007-2013) under grant agreement no. 312789.

REFERENCES

Arnaud K. A., 1996, in Jacoby G., Barnes J., eds, ASP Conf. Ser. Vol. 101, Astronomical Data Analysis Software and Systems V. Astron. Soc. Pac., San Francisco, p. 17
Ballantyne D. R. et al., 2014, ApJ, 794, 62
Baloković M. et al., 2015, ApJ, 800, 62
Barthelmy S. et al., 2005, Space Sci. Rev., 120, 143
Baumgartner W. H., Tueller J., Markwardt C., Skinner G., Mushotzky R., 2011, Am. Astron. Soc. Meeting Abstr., 218, 328.11
Bowen Ira S., 1960, ApJ, 132, 1
Brenneman L. W. et al., 2014, ApJ, 781, 83
Dadina M., 2007, A&A, 461, 1209
Fabian A. C., 1994, ApJS, 92, 555
Fabian A. C., Lohfink A., Kara E., Parker M. L., Vasudevan R., Reynolds C. S., 2015, MNRAS, 451, 4375
Ferland G. J. et al., 2013, Rev. Mex. Astron. Astrofis., 49, 137
Gabriel C. et al., 2004, in Ochsenbein F., Allen M. G., Egret D., eds, ASP Conf. Ser. Vol. 314, Astronomical Data Analysis Software and Systems (ADASS) XIII. Astron. Soc. Pac., San Francisco, p. 759
García J. et al., 2014, ApJ, 782, 76
Gehrels N. et al., 2004, ApJ, 611, 1005
Guainazzi M., Bianchi S., de La Calle Pérez I., Dovčiak M., Longinotti A. L., 2011, A&A, 531, A131
Haardt F., Maraschi L., 1993, ApJ, 413, 507
Harrison F. A. et al., 2013, ApJ, 770, 103
Kalberla P. M. W., Burton W. B., Hartmann D., Arnal E. M., Bajaja E., Morras R., Pöppel W. G. L., 2005, A&A, 440, 775
Kallman T., Bautista M., 2001, ApJS, 133, 221
Keek L., Ballantyne D. R., 2016, MNRAS, 456, 2722
La Franca F. et al., 2015, MNRAS, 449, 1526
Laor A., Behar E., 2008, MNRAS, 390, 847
Magdziarz P., Zdziarski A. A., 1995, MNRAS, 273, 837
Maiolino R., Marconi A., Salvati M., Risaliti G., Severgnini P., Oliva E., La Franca F., Vanzi L., 2001, A&A, 365, 28
Malizia A., Molina M., Bassani L., Stephen J. B., 2014, ApJ, 782, L2
Marconi A., Risaliti G., Gilli R., Hunt L. K., Maiolino R., Salvati M., 2004, MNRAS, 351, 169
Marinucci A. et al., 2014, MNRAS, 440, 2347
Martí J., Mirabel I. F., Chaty S., Rodriguez L. F., 1998, A&A, 330, 72
Matt G. et al., 2015, MNRAS, 447, 3029
Mewe R., Gronenschild E. H. B. M., van den Oord G. H. J., 1985, A&AS, 62, 197
Miller J. M., Parker M. L., Fuerst F., 2013, ApJ, 775, L45
Miller J. M., Tomsick J. A., Bachetti M., 2015, ApJ, 799, L6
Molina M., Bassani L., Malizia A., Stephen J. B., Bird A. J., Bazzano A., Ubertini P., 2013, MNRAS, 433, 1687
Nandra K., George I. M., 1994, MNRAS, 267, 974
Nandra K., O'Neill P. M., George I. M., Reeves J. N., 2007, MNRAS, 382, 194
Pavlinsky M. N., Grebenev S. A., Sunyæv R. A., 1992, Sov. Astron. Lett., 18, 217
Perola G. C., Matt G., Cappi M., Fiore F., Guainazzi M., Maraschi L., Petrucci P. O., Piro L., 2002, A&A, 389, 802
Petrucci P. O. et al., 2000, ApJ, 540, 131
Petrucci P. O. et al., 2001, ApJ, 556, 716
Piccinotti G., Mushotzky R. F. Boldt E. A., Holt S. S., Marshall F. E., Serlemitsos P. J., Shafer R. A., 1982, ApJ, 253, 485
Piconcelli E., Jimenez-Bailón E., Guainazzi M., Schartel N., Rodríguez-Pascual P. M., Santos-Lleó M., 2004, MNRAS, 351, 161
Poutanen J., Svensson R., 1996, ApJ, 470, 249
Protassov R., van Dyk D. A., Connors A., Kashyap V. L., Siemiginowska A., 2002, ApJ, 571, 545
Ricci F., La Franca F., Onori F., Bianchi S., 2016, A&A, preprint (arXiv:1610.03490)
Rybicki G. B., Lightman A. P., 1979, Radiative Processes in Astrophysics. Wiley-Interscience, New York
Sakano M., Koyama K., Murakamu H., Maeda Y., Yamauchi S., 2002, ApJS, 138, 19
Sazonov S. Yu., Revnivtsev M. G., 2004, A&A, 423, 469
Sazonov S. Yu., Revnivtsev M. G., Lutovinov A. A., Sunyaev R. A., Grebenev S. A., 2004, A&A, 421, 21
Shakura N. I., Sunyæv R. A., 1973, A&A, 24, 337
Shemmer O., Brandt W. N., Netzer H., Maiolino R., Kaspi S., 2006, ApJ, 646, L29
Sobolewska A., Papadakis I. E., 2009, MNRAS, 399, 1597
Strüder L. et al., 2001, A&A, 365, L18
Titarchuk L., 1994, ApJ, 434, 570

Tombesi F., Cappi M., Reeves J. N., Palumbo G. G. C., Yaqoob T., Braito V., Dadina M., 2010, A&A, 521, A57
Turner M. J. L. et al., 2001, A&A, 365, L27

APPENDIX A: BLACK HOLE MASS ESTIMATE

The spectroscopic observation of the optical counterpart of GRS 1734−292 was carried out with the ESO Faint Object Spectrograph and Camera (v.2) instrument mounted on the 3.6 m European Space Agency New Technology Telescope (ESO-NTT) at La Silla, on 2010-07-08 (programme ID:085.D-0441(C), PI: Jonker), using GRating prISM 13 and a 1 arcsec slit. The pointing is 500 s long and we used IRAF (version 2.16) and MIDAS (release 15SEPpl1.0) for data reduction and calibration, using standard procedures.

The aim of our analysis was to measure the width of the broad Hα λ6563 component, to infer the black hole mass via a virial-based, single-epoch relation (La Franca et al. 2015; Ricci et al. 2016). In Figs A1 and A2, the 4700–7500 and 6500–7500 Å spectra of GRS 1734−292, respectively, are shown: several emission lines of H, O, N and S elements can be clearly seen. Throughout our analysis, we assumed that F([N II] λ6583)/F([N II] λ6548) = 3, as required by the ratio of the respective Einstein coefficients. Spectra are fitted with XSPEC, via χ^2 minimization, by modelling the continuum as a power law convolved with a SPLINE function, and each line component as a Gaussian. The width of the narrow lines was fixed to the instrumental one, inferred from fitting the He–Ar calibration lines. We assumed a redshift $z = 0.0214$ (Martí et al. 1998) and that all reported wavelengths in Table A1 are rest frame. The inferred fluxes for the Hα (broad component) and Hβ emission lines lead to an observed Hα/Hβ > 12.6. Assuming an average Balmer-line intensity relative to Hβ of 2.86 (case B recombination), we calculate a Galactic extinction in the V band of $A_V > 4.6$ mag. Adopting the standard Galactic gas-to-dust ratio, the optical reddening may be rewritten using the relation $A_V = 5.27 N_{\rm H}^{22}$ mag, where the absorbing column density is expressed in units of 10^{22} cm^{-2} (see e.g. Maiolino et al. 2001, and references therein). The lower limit obtained with the optical data analysis is in agreement with the absorbing column density measured from the X-ray spectrum.

We measured an FWHM = 4940 ± 50 km s^{-1} for the broad component of the Hα line. This value and the 2–10 keV luminosity measured with *XMM–Newton*, which is the closest observation in time ($L_X = 5.23 \pm 0.03 \times 10^{43}$ erg s^{-1}), allow us to use the updated calibrations of the virial black hole mass estimators (Ricci et al. 2016). The inferred mass is $\log(M_{\rm bh}/{\rm M}_\odot) = 8.5$, with an intrinsic spread of the relation of ∼0.5 dex.

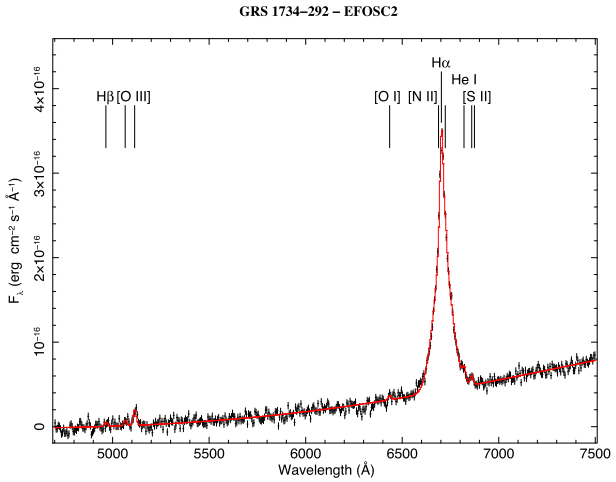

Figure A1. ESO-NTT optical spectrum of the source, in the 4700–7500 Å range. Emission lines from several elements such as H, O, N and S are clearly detected.

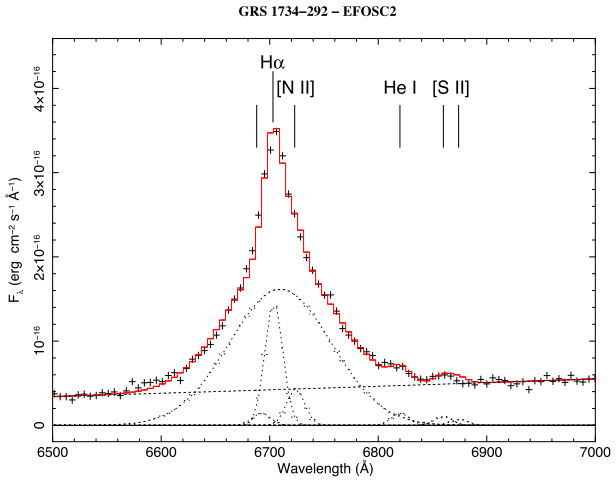

Figure A2. ESO-NTT optical spectrum of the source, in the 6500–7500 Å range.

Table A1. Optical emission lines in the ESO-NTT spectrum of GRS 1734−292.

Line (1)	λ (2)	Flux (3)	FWHM (4)
Hβ	4861.33	<1.5	–
[O III]	4958.92	0.13 ± 0.08	–
[O III]	5006.85	0.38 ± 0.08	–
[O I]	6300.32	0.10 ± 0.08	–
[N II]	6548.06	0.30 ± 0.03	–
Hα Nr.	6562.79	$3.02^{+0.06}_{-0.13}$	–
Hα Br.	6562.79	$19.03^{+0.26}_{-0.20}$	4940 ± 50
[N II]	6583.39	0.90 ± 0.09	–
He I	6678.11	0.3 ± 0.1	–
[S II]	6716.42	0.20 ± 0.07	–
[S II]	6730.78	0.15 ± 0.05	–

Notes. Column (1): identification. Column (2): laboratory wavelength (Å) (air: Bowen 1960). Column (3): fluxes in 10^{-15} erg cm^{-2} s^{-1} units. Column (4): FWHM in km s^{-1} units. Dashes indicate a fixed FWHM = 18 Å.

This paper has been typeset from a TEX/LATEX file prepared by the author.